



Combustion in a Meso-Scale Liquid-Fuel-Film Combustor with Central-Porous Fuel Inlet

Yueh-Heng Li , Yei-Chin Chao & Derek Dunn-Rankin

To cite this article: Yueh-Heng Li , Yei-Chin Chao & Derek Dunn-Rankin (2008) Combustion in a Meso-Scale Liquid-Fuel-Film Combustor with Central-Porous Fuel Inlet, Combustion Science and Technology, 180:10-11, 1900-1919, DOI: [10.1080/00102200802261464](https://doi.org/10.1080/00102200802261464)

To link to this article: <http://dx.doi.org/10.1080/00102200802261464>



Published online: 02 Oct 2008.



Submit your article to this journal [↗](#)



Article views: 117



View related articles [↗](#)



Citing articles: 12 View citing articles [↗](#)

COMBUSTION IN A MESO-SCALE LIQUID-FUEL-FILM COMBUSTOR WITH CENTRAL-POROUS FUEL INLET

Yueh-Heng Li¹, Yei-Chin Chao¹, and Derek Dunn-Rankin²

¹Institute of Aeronautics and Astronautics, National Cheng Kung University
Tainan, Taiwan, ROC

²Institute of Mechanics and Aeronautics, University of California, Irvine,
California, USA

Utilizing a metal-porous medium for a liquid fuel film combustor is an effective method to increase the contact surface area and conduction heat transfer for liquid fuel vaporization and flame stabilization. Based on this concept, a meso-scale liquid fuel film combustor with a central porous inlet is developed and tested. The effects of porous material type and bead size on the flame structures and combustion characteristics are examined. Porous media made of stainless steel and bronze are tested in the meso-scale combustor with different fuel and air flow rates, equivalence ratios, and bead sizes. The flame structure and its corresponding stabilization mechanism are different between the stainless steel and the bronze porous media combustor. In the stainless steel case, the high specific heat capacity enhances fuel vaporization and fuel-air mixing, and the flame anchor locates on the surface of the porous cap. In the bronze case, due to its low heat capacity, the flame is swept downstream where the recirculation zone above the porous cap offers a low velocity field to help anchor the flame. The flame structure and stabilization mechanism in the chamber can be related to a tribrachial flame. Chemiluminescence measurement and Abel deconvolution are performed to verify the flame structure in the vicinity of the porous cap. In addition, temperature measurements and exhaust gas analysis highlight the differences in combustion characteristics between the two kinds of porous media. As regards bead size effects, results indicate that there is no obvious difference in flame structure and flame anchoring position, but the stable operating ranges of a porous combustor decrease with decreasing bead size due mainly to the concomitant increase in thermal conductivity.

Keywords: Chemiluminescence; Liquid film fuel; Mesoscale combustor; Porous media

INTRODUCTION

Over the past decade, valuable combustion research has been inspired by the demand to create small-scale or micro-scale heat engines capable of producing power in the 10–100 W range. Utilizing combustion for power generation in micro or meso systems is motivated by the fact that the stored energy density of hydrocarbon fuels is greater than that achievable by the current battery technology (e.g., ~45 MJ/kg for liquid heptane versus 0.6 MJ/kg for Lithium-Ion battery). Furthermore, the

Received 1 October 2007; accepted 17 February 2008.

Address correspondence to Yei-Chin Chao, Institute of Aeronautics and Astronautics, No.1, Ta-Hsueh Rd., Tainan, 701, Taiwan, ROC. E-mail: ycchao@mail.ncku.edu.tw

specific power potential from combustion is far higher than can be achieved with surface mediated electrochemical reactions. With the large energy densities of hydrocarbon fuels, combustion-based micro power devices can be competitive over contemporary lithium batteries, even if the overall efficiency is as low as 10% (Fernandez-Pello, 2003). As a result, combustion based power generators are considered to be a promising solution to meet the need for a compact high energy and power density source. The recent interest in personal power systems further underscores the needs for compact, efficient, human compatible, lightweight power sources (Dunn-Rankin et al., 2005).

Although much of the early and current researches on small-scale power generation systems have focused on micro-scale systems (Spadaccini et al., 2003; Norton and Vlachos, 2005; Yuasa et al., 2005), meso-scale combustion has received increasing attention in recent years due to its potential applications. Low-cost meso-scale or miniature heat engines can provide high thermal efficiency and longevity for targeted applications. Nevertheless, combustion at small-scales is still a topic of significant fundamental and practical importance. The relatively high reactant mass flow rate needed to achieve high energy density at small-scales shortens the residence time for liquid fuel vaporization, fuel-air mixing and chemical reactions. Inadequate vaporization, non-uniform fuel-air mixing and poor combustion degrade the overall system performance.

Moreover, the large surface area-to-volume ratio of small-scale combustor increases surface heat loss, which is generally responsible for flame quenching and poor thermal efficiency. Therefore, several concepts to achieve stable combustion at small scales have been proposed to overcome these difficulties. Weinberg et al. (2002) proposed a Swiss-roll design to recycle product gas energy to preheat and thereby increase the reaction rates in small-scale combustion systems. Ahn et al. (2005) investigated both gas-phase and catalytic combustion in the Swiss-roll design and found that the catalytic combustion greatly increased the reaction rates, especially at low reactant flow rates. Wang et al. (2004) utilized swirl-stabilized combustion for meso-scale applications, and investigated the role of the recirculation zone in stabilizing the flame. For liquid fuels, Kaiser et al. (2003) and Kyritsis et al. (2004) developed a meso-scale catalytic combustor using electrostatic spray for fuel atomization.

Sirignano et al. (2002, 2005) proposed the concept of a liquid fuel film, with the liquid fuel flowing directly on the combustor wall, not only to reduce heat loss but also to improve fuel vaporization. Liedtke and Schultz (2003) proposed a similar concept with the liquid fuel film on the inner surface of a tube and combustion products in an annulus around the tube. Marbach and Agrawal (2005) introduced a heat recirculating combustor with the flame stabilized on the surface of a Silicon-Carbide (SiC) coated carbon foam used as the porous inert media (PIM). Kaplan and Hall (1995) and Tseng and Howell (1996) proposed a porous inert burner of liquid fuel atomized by a high-pressure injector. It appears, therefore, that the porous burner is less efficient as compared to the conventional spray burner, in part because the full potential of the porous media has not yet been extended, enhance the evaporation process.

On the other hand, an experiment of an up-flow, non-spray porous inert media burner was attempted (Fuse et al., 2005) with evaporation completely within the porous burner. However, in the experiment the combustion occurred outside the porous burner at its downstream end. A method allowing both evaporation

and combustion to occur within a porous burner is of special importance for its potentially high combustion efficiency and high radiation output for practical applications, such as thermophotovoltaic (TPV) cells in combustion-driven radiant combustors (Durish et al., 2003; Qiu and Hayden, 2007).

Considered to enhance the overall efficiency of combustion-driven power system, stable and complete combustion in small configurations appears significant and difficult. Similarly, attention to the flame stabilization mechanism in a small combustor is essential. Kim et al. (2005) claimed that the open combustion space located in the center of swiss-roll combustor enhances the flow divergence or flow recirculation near the inlet to the combustion zone, and explained that this is a vital parameter in the design of a swiss-roll combustor. As to porous inert media burners, the flame is generally stabilized inside the combustion chamber on the downstream surface of the porous inert media (Marbach, 2007). In a fuel-film combustor, Pham et al. (2007) described the fuel-film flame as being composed of two structures: a double flame at the exit rim and a central tribrachial flame within the chamber which provide as stable ignition site.

CONCEPT

Based on the results described in these prior works, we consider a central porous fuel inlet combustor in order to confine a liquid-fueled flame inside a small chamber and also to preheat the liquid fuel. When burning liquid fuels in miniature combustors, the optimal choice is to inject all or a portion of the fuel directly as a film on the solid surfaces where high heat transfer from the combustion products occurs. The major purpose of designing the combustor, therefore, is that liquid fuel can be spread over a chosen surface through porous materials on account of its own momentum and surface tension, as well as friction forces from neighboring flowing gases, and gravity. On the other hand, the interface between liquid fuel and chamber wall is supposed to offer the liquid fuel sufficient energy for latent and sensible heat immediately and efficiently by any form of heat transfer from the flame and hot product gas.

In general, porous media have sufficiently high porosity to let the surface tension force spread the liquid fuel over the wall uniformly and completely. In addition, metallic porous media inherently possesses excellent heat recuperation by radiation and thermal conduction. Applying a porous cap in the core of a miniature combustor might then not only meet the requirement of forming the fuel film, but also help directly vaporize the liquid film from the metallic porous surface.

In this paper, the flame structures and combustion characteristics in the proposed central porous combustor with different porous materials and bead sizes are studied using chemiluminescence techniques and by analyzing the flame structure and its anchoring position, the flame stabilization mechanism in the central porous liquid fuel-film combustor is described.

EXPERIMENTAL SETUP

Figure 1 shows the schematic of the meso-scale liquid film combustion chamber. The main chamber and a liquid-fuel trough are separated by a porous cap.

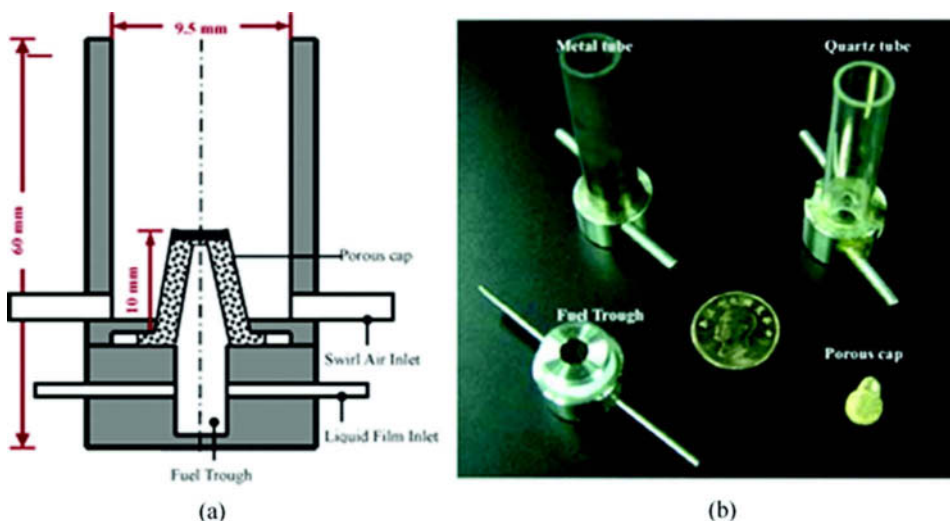


Figure 1 (a) Schematic diagram of the experimental combustor and (b) a photograph of the experimental combustor.

Normal heptane fuel is injected smoothly from two inlet ports into the fuel trough using a syringe pump, which provides continuous fuel inlet at low flow rate. The air, metered by an electronic flowmeter, is injected tangentially above the fuel ports. Swirling air entering a cylindrical chamber draws liquid fuel out and generates a liquid film on the porous surface. It also provides a mechanism (recirculation) whereby the flame can be stabilized. The swirl system is used mainly to enhance mixing and increase residence time in the small-scale combustor in order to overcome the detrimental effects on reaction due to the large surface-to-volume ratio.

Furthermore, liquid fuel passing through the porous media has the large contact area needed for vaporization, and metallic porous media can absorb heat from the flame and effectively conduct this heat to the liquid fuel for evaporation. In this way, the porous cap not only supplies a liquid-film-surface area large enough to produce necessary fuel vaporization rates but also provides heat recuperation between the liquid fuel and the flame.

The combustion chamber consists of three parts: (1) the main combustion chamber of 9.5 mm inside diameter (ID) with swirling air inlet ports, (2) a base chamber set with a fuel trough of 10 mm ID and fuel inlet ports, and (3) a porous fuel-injection cap, as shown photographically in Figure 1b. The main chamber is made of 304 stainless steel (or a quartz tube for visualization), and is 60 mm in length with a wall of 1 mm thickness. Two materials are used for the porous media, stainless steel and bronze, with the same bead size for both ($\sim 20\ \mu\text{m}$). We also study three different bead sizes in the bronze porous cap only, 20, 40 and $70\ \mu\text{m}$ to examine bead size effects. All porous media have a similar truncated conical shape; its dimension is 4 mm in diameter on top and 6.5 mm in diameter at the bottom, which a 10 mm length.

Liquid n-heptane fuel is supplied by a continuous syringe pump. Air is supplied by an air compressor, then dried and metered with a mass flowmeter calibrated

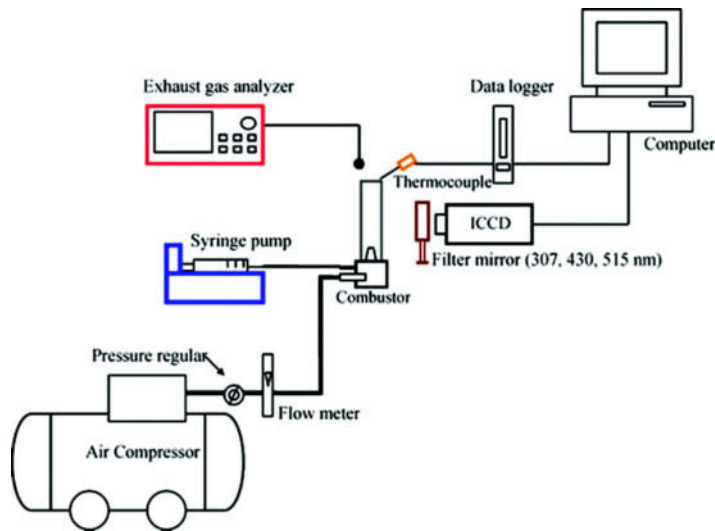


Figure 2 Experimental setup of the central-porous combustor.

in the range of 0–60 standard l/min. The exit temperature is measured by a R-type thermocouple with 0.075 mm bead diameter located in the vicinity of the chamber end plane. Figure 2 shows the measurement instruments used in this work. The exit temperature is recorded uncorrected for radiation, by a NI DAQ card. The uncertainty of the temperature measurement is estimated to be 20 K.

Concentrations of NO_x and CO were measured with infrared gas analyzers (MRU VarioPlus) calibrated in the range of 0–600 ppm with an uncertainty of ± 2 and ± 5 ppm, referring to 15% O_2 , respectively. The chemiluminescence images are taken with their respective narrow bandpass filters through a 14-bit intensified CCD camera at wavelengths of 307 nm for OH^* , 430 nm for CH^* and 515 nm for C_2^* .

RESULTS AND DISCUSSION

Combustion in Combustor of Different Porous Materials

Flame phenomenology. The thermal conductivity and specific heat of a central porous medium should significantly influence the thermal recuperating mechanism of a meso-scale combustor. Figure 3 shows that, the flame anchoring point using a stainless steel porous material is different from that using bronze porous material with the same bead size. The flame structure with the bronze porous medium combustor shows two layers of flame; one is the inner flame acting like a pilot flame, and the other is the outer flame behaving as a swirl flame. The flame base locates in the vicinity of the cap top of the porous medium.

No significant change in flame anchoring and flame structure can be found in Figure 3 as the air flow rate is increased. For the stainless steel porous medium, the flame structure looks like a swirl flame and the flame base anchors on the lateral surface of the porous cap as well as at the tube exit. When the air flow rate increases,

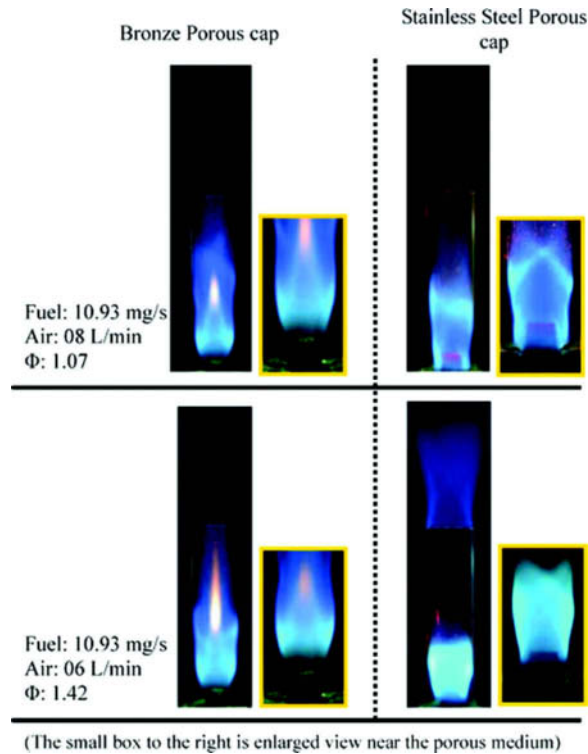


Figure 3 Flame mode and flame anchor position for different porous materials.

the exit flame moves upstream. The red hot spot on the stainless steel cap also becomes larger and brighter with increasing air flow rate.

Apparently, there are different flame stabilization mechanisms for the two different porous material cases. Interestingly, tracing the flame anchor locations, as shown in Figure 4, shows that for the stainless steel case the flame first locates on top of the porous cap (which is similar to the bronze case) and then the flame proceeds upstream and stabilizes on the lateral surface about -3 mm from the top of the porous cap, for the case of air flow at 6.5 L/min and the fuel flow of 10.93 mg/sec. In contrast, the flame for the bronze porous case stays fairly still at 1.3 mm above the porous cap throughout the flow range. Different flame structures and anchoring behaviors imply different flame stabilization mechanisms.

Figure 5 shows the stable operating window in terms of fuel and air flow rates for a central-porous combustor of different porous materials. The upper limit of the operating window is flame blow-off or extinction, and the lower limit is defined by flame quenching or something we call the flame volcano condition. The flame volcano is caused by excess liquid fuels or low swirl air. Low swirl air is unable to spread the liquid fuel over the tube wall so it accumulates as a fuel pool in the bottom of the combustor. Eventually, fuel drops splash out by flame heating and boiling the liquid. We do not consider this situation as stable combustion. Based on the above limits definition, the operating window of a bronze porous

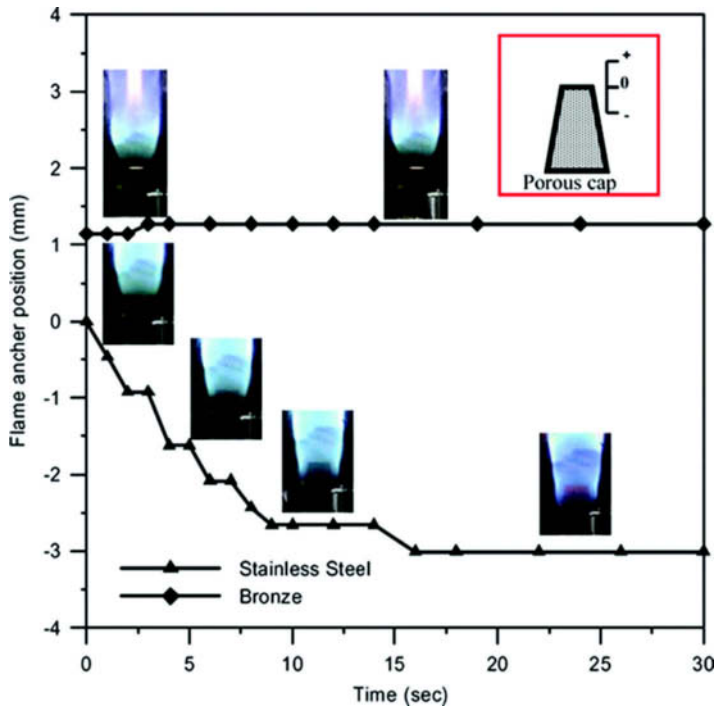


Figure 4 Movement of the flame anchor position in stainless steel and bronze cases.

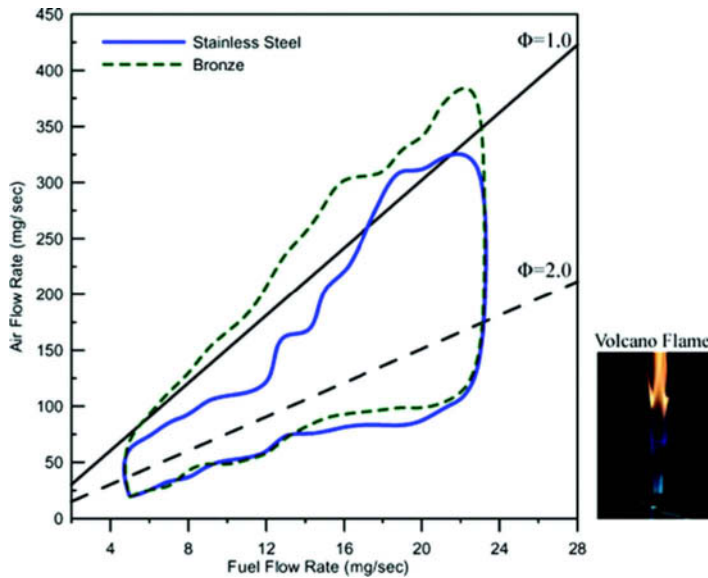


Figure 5 Stable operating envelopes for the combustor with different porous materials.

medium combustor is much wider than that of a stainless steel porous medium combustor.

Furthermore, Figure 5 indicates that a bronze porous medium combustor has the capability of operating in the fuel-lean regime while the stainless steel porous medium combustor burns stably only in the fuel-rich regime. In general, stainless steel has a lower thermal conductivity (16.2 W/m-K) so that its temperature takes longer to reach a new equilibrium condition. Moreover, stainless steel also has smaller thermal diffusivity ($\sim 4.05 \times 10^{-6} \text{ m}^2/\text{s}$) and is better able to store heat from flames. Hence, as shown in Figure 3, there is a hot spot on top of the stainless steel porous cap when the combustor runs stably. Although the hot spot can successfully provide a heat source for fuel vaporization, an over-heated porous medium triggers combustion instabilities. Typical combustion instabilities bring in periodic flame pulsations, and even flame blow-off. Therefore, excess liquid fuel is necessary to cool down the porous material.

This explains why the stainless steel combustor generally runs stably in the fuel-rich regime and why it can run stably near the stoichiometric condition only in high fuel flow rates (up to 16 mg/sec) conditions. The higher liquid fuel supply maintains the proper temperature of the porous medium for stable combustion. As to bronze porous medium combustor, the stable operating area extends to the fuel-lean regime and the flame stabilizes above the porous medium. It appears that a recirculation zone near the top of a porous cap helps to stabilize the flame. Whenever the air flow rate rises, the flame anchor remains unmoved, a small distance away from porous top.

Bronze has somewhat higher thermal conductivity ($\sim 385 \text{ W/m-K}$) and its thermal diffusivity ($\sim 1.12 \times 10^{-4} \text{ m}^2/\text{s}$) is almost two orders of magnitude higher than that of stainless steel. Hence, for bronze, the heat from a flame would effectively conduct away from the surface and be absorbed by the liquid fuel. There is no hot spot in this case, and combustion instability rarely occurs. These results show that the flame stabilization mechanisms are distinct and different for the two porous materials even when their bead sizes are equal.

As indicated above, in the stainless steel porous combustor, a hot spot offers a flame stabilization mechanism because it locally accelerates liquid fuel vaporization. The produced fuel vapor then mixes with fresh swirling air near the porous cap, leading to rapid reaction along the lateral surface of the cap. Similar to flame spread along a flat plate, it seems that the flame stabilization mechanism in the stainless steel porous combustor is related to the tribrachial flame structure, see Figure 6a. For the tribrachial flame structure, there is a diffusion flame (DF) between the chamber wall and the porous cap, with the diffusion flame twisted by the swirl air. A rich premixed flame (RPF) leans on the porous cap and a lean premixed flame (LPF) winds with the diffusion flame along the chamber.

The flame anchoring point occurs where there is a balance between the propagation rate of apex point of the tribrachial flame and the supply of the fuel/air mixture which then balances the supply and consumption of flammable (or stoichiometric) fuel-air mixture. Occasionally, the stainless steel hot spot can influence the balance which is one cause for flame flickering as it occasionally moves forward and backward.

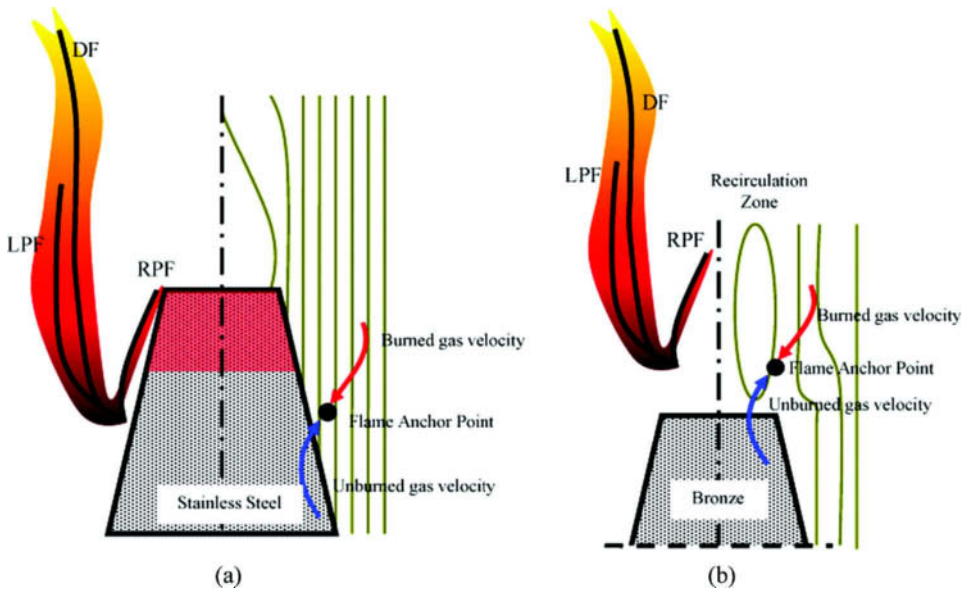


Figure 6 Proposed tribrachial flame structures for the (a) stainless steel and (b) bronze porous media combustors.

On the other hand, in the bronze porous case, the flame is stationary on top of the porous cap. The bluff body nature of the porous cap produces a recirculation zone behind it. The recirculation zone provides a relative low velocity field so that the flame base anchors in this area, as shown in Figure 6b. There is still a tribrachial flame stabilization mechanism, however. In the bronze porous combustor, a diffusion flame (DF) and a lean premixed flame (LPF) twist and burn along the chamber wall, while a rich premixed flame (RPF) inclines to the symmetrical axis of the chamber. The flame anchoring position is quite stable due to the high thermal conductivity of a bronze. Hence, despite different flame anchoring phenomena, the flame stabilization mechanism in combustors of two different porous materials is mainly a typical tribrachial flame.

Combustion Stabilization Mechanism

In order to further verify the mechanism of flame stabilization, chemiluminescence imaging is performed. The chemiluminescent emissions of OH^* , CH^* and C_2^* in hydrocarbon flames can be related to the chemical reaction rate and heat release rate (Najm et al., 1998; Lawn, 2000; Cheng et al., 2006). Specifically, C_2^* is a short-lived radical, which is a good indicator of highly rich reaction zones while CH^* is a longer-lived radical describing the broader zone of reaction rather than just the reactive interface (Shu, 1998; Qin, 2002). Therefore, determining some particular radicals including OH^* , CH^* and C_2^* can help to delineate the flame structure near the porous cap.

OH^* , CH^* and C_2^* images were taken using their respective narrow bandpass filters through a 14-bit intensified CCD camera at wavelengths of 307, 430, and 515 nm,

respectively. The combustor was tested at an airflow rate of 8 L/min and a heptane flow rate of 10.93 mg/s, for a resulting equivalence ratio of 1.07. Since the chamber has a cylindrical geometry, direct images of the flame integrate emission along the line of sight, and will not accurately represent the planar radical distribution. Appropriate analysis of the images requires deconvolution of the integrated image into a planar image. This can be accomplished by applying the inverse Abel transform.

Solving the linear Abel equation in a cylindrically symmetric geometry will result in the equation

$$F(r_i) = \frac{1}{\Delta r} \sum_{j=0}^{\infty} D_{ij} p(x_j)$$

where r_i is the distance from the center of the object, $F(r_i)$ is the radial field distribution, Δr is the spacing between lines of sight, D_{ij} is the matrix of linear operator coefficients, and $p(x_i)$ is the line of sight projection data. The three-point Abel deconvolution recommended by Dasch (1992) is one of the easiest and fastest to calculate, and has the lowest noise. The three-point Abel deconvolution breaks the Abel integral into segments around each point r_i .

In the neighborhood of each point, $p(x_i)$ is expanded quadratically using only the projections adjacent to r_i . Figure 7 shows the CH* chemiluminescence

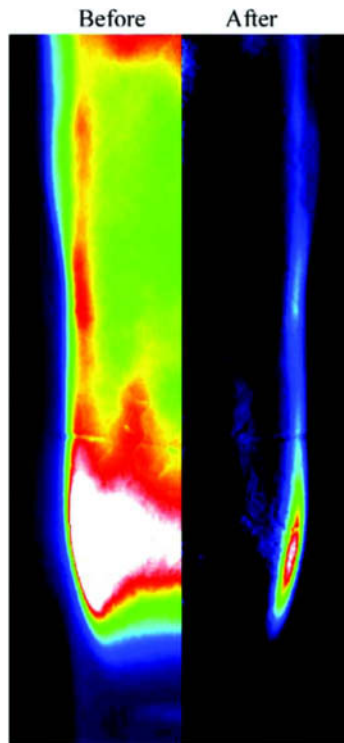


Figure 7 CH* chemiluminescence image before and after Abel deconvolution.

image before and after Abel deconvolution. On the left-hand side of Figure 7, the line-of-sight integrated image appears to show that the radical concentration mostly congregates in the bottom of the flame. After Abel deconvolution (right-hand side of Figure 7), however, the image shows that the radical concentrations distribute in two layers and peaks at a location corresponding to the expected flame characteristics.

Figure 8 presents the radical concentration images of OH^* , CH^* , C_2^* and the corresponding flame image near the stainless steel porous cap. The flame anchors in the vicinity of the porous surface, with two distinct flame layers, as shown in Figure 8a. One layer extends along the porous cap and the other along the wall. C_2^* radicals are distributed in the two flame layers and their concentration peaks in the layer along the wall, as shown in Figure 8b. The C_2^* radical concentration indicates highly rich zones in these regions. In contrast, the OH^* concentration is high near the wall and it fades away toward the porous medium (Figure 8d), revealing the main reaction zone near the wall.

Moreover, CH^* radicals are extensively congregated in the regions near the wall and near the porous medium (Figure 8c). The two concentration branches overlap at the point close to the flame base near the porous surface. These images confirm that the flame structure is composed of two-layer flames in the chamber consisting of a lean and a rich premixed flame wings together with a trailing diffusion flame. All of these flames extend from a single point at the flame base, which corresponds to the stabilization point of the tribrachial flame which anchors the flame. A diffusion flame burns between the wall and the porous cap. A rich premixed flame exists close to porous cap and forms a boundary-layer-like flame sheet along it. The lean premixed flame of the tribrachial structure is difficult to see due to its low luminosity, but it can vaguely be identified near the wall.

Figure 9 shows the deconvoluted radical images of OH^* , CH^* , C_2^* and their corresponding flame image near the bronze porous cap. The OH^* , CH^* and

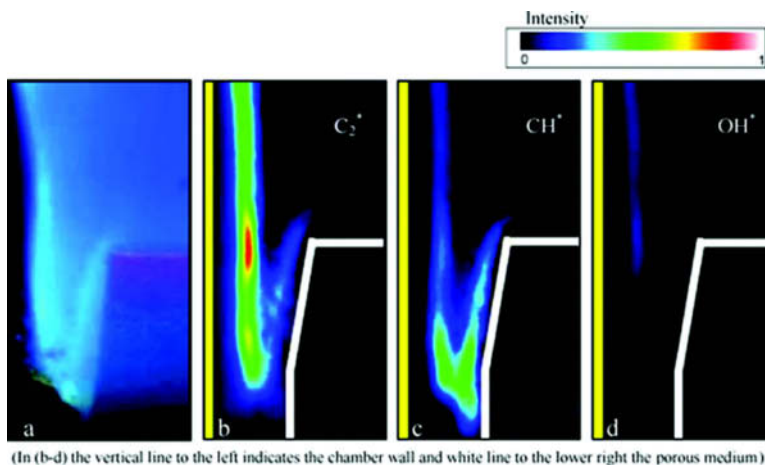


Figure 8 Chemiluminescence images of OH^* , CH^* and C_2^* next to a photograph of the corresponding flame in stainless steel porous medium combustor.

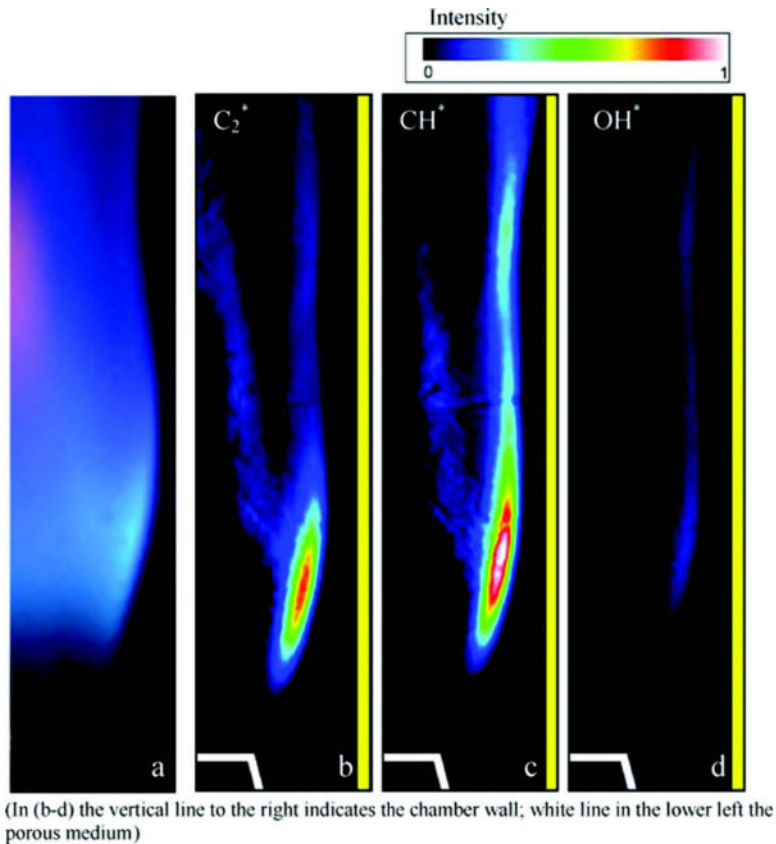


Figure 9 Chemiluminescence images of excited OH^* , CH^* and C_2^* next to a photograph of the corresponding flame in the bronze porous medium combustor.

C_2^* radicals distribute in two flame layers as shown in Figures 9b–9d. The flame structure looks similar to that of the stainless steel case, except that the flame anchors above the porous cap. A diffusion flame layer, depicted by peak CH^* and C_2^* radical concentrations and main OH^* distribution, can easily be identified. A fuel rich flame separates from the diffusion flame's base and leans toward the axis of symmetry to form a pilot flame above the porous cap. The stabilization point of the tribrachial flame base locates in the recirculation zone atop the bronze porous cap as shown schematically in Figure 6b.

Emission Measurements

Figure 10 presents the measured temperature profiles at the combustor exit plane for stainless steel and bronze porous combustors. The right-hand side of Figure 10a shows the exit temperature distribution of the bronze porous combustor for the case of 6 L/min air flow rate and $\Phi = 1.42$; the left-hand side shows the temperature for the stainless steel porous combustor at identical air/fuel conditions. The resultant profile at the combustor exit shows a parabolic shape with the highest

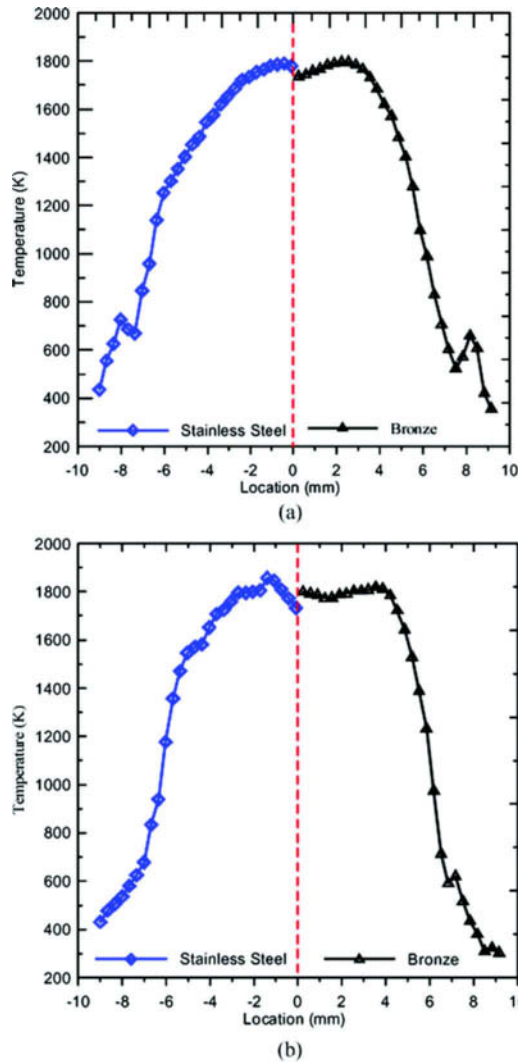


Figure 10 Temperature distribution at the combustor exit in the conditions of: (a) air 6 L/min and fuel 10.92 mg/sec, and (b) air 8 L/min and fuel 10.92 mg/sec. (in the figure, right-hand side for the case of stainless steel and left-hand side for bronze porous media).

gas temperature around the midpoint and lower values adjacent to the ambient. The temperature peak at the exit of the stainless steel porous combustor locates closer to the chamber axis than does that of the bronze porous combustor.

There is a small temperature jump at the outer edge of the chamber. The jump in flame temperature at the outer edge of the chamber reveals that the unburned gas could combust again at the rim of the chamber in fuel-rich cases as it contacts fresh oxidizer. When the air flow rate rises to 8 L/min, corresponding to $\Phi = 1.07$, the outer-edge temperature jump becomes small or even disappears. The temperature profile of the stainless steel case shows a twin peak shape (shown in the LHS of

Figure 10b), and the temperature profile of the bronze case has a top-hat shape. The temperature profiles correspond to their respective flame structures. The twin peak profile indicates a swirl flame in the stainless steel case, and the top hat profile is caused by twinkling of the two-layer flame (see Figure 3).

Assuming the velocity and mass distribution profiles are unknown, that the composition and mass flux per unit area are uniform, and that the area-averaged temperature based on the measured temperature profile can be calculated, the combustion efficiency relative to a stoichiometric flame can be computed. Since the efficiency can be defined as $\eta = \dot{m}_{fuel, burned} / \dot{m}_{fuel}$, and the approximation can be made that $\dot{m}_{fuel, burned} / \dot{m}_{fuel, stoich} = T_{mean} / T_{adiabatic}$, the efficiency is estimated as

$$\eta = \frac{T_{mean}}{T_{adiabatic} \times \phi}$$

where ϕ is the equivalence ratio.

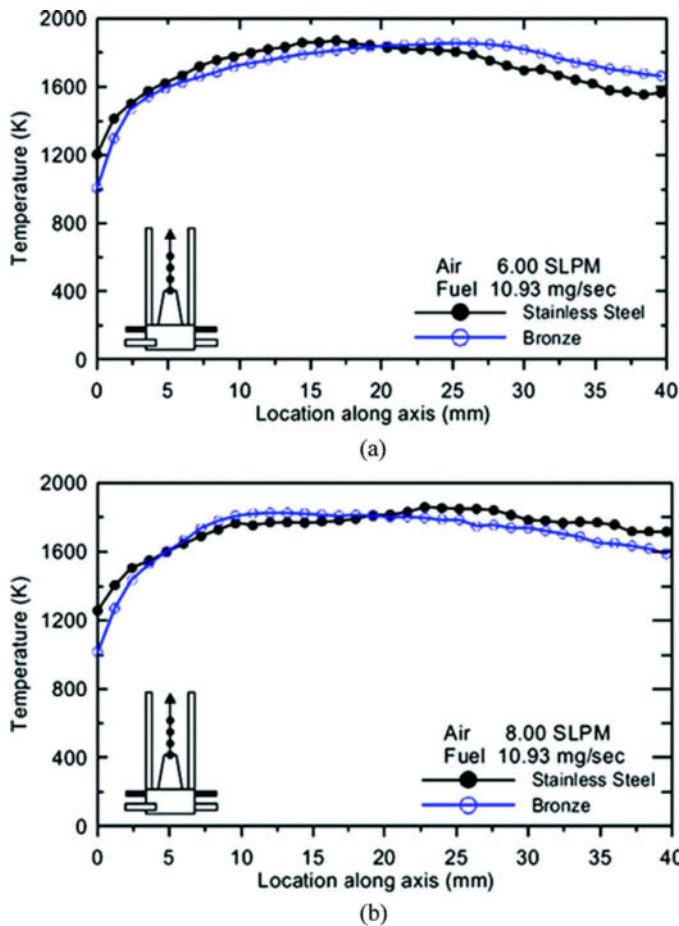


Figure 11 Temperature distribution along the axis of the combustor in the conditions of: (a) air 6 L/min and fuel 10.93 mg/sec and (b) air 8 L/min and fuel 10.93 mg/sec.

Accordingly, $T_{adiabatic}$ for n-heptane is 2050 K in air of 6 L/min and fuel of 10.92 mg/sec, and its corresponding equivalence ratio is 1.42. The efficiency of the stainless steel porous media combustor is estimated to be 59% and the efficiency of bronze porous media combustor is 62%. When the air flow rate is 8 L/min and fuel is 10.92 mg/sec ($\phi = 1.28$), the efficiency improves to 67% in the stainless steel case and 69% in a bronze case, based on $T_{adiabatic} = 2132$ K. Generally, the internal combustion efficiency of the bronze porous media combustor is a little higher than that for a stainless steel porous media combustor, even if the air flow rate increases. The relatively lower efficiency at low flow rate seems reasonable since the combustor displays evidence of a flame attaching on its exit rim at these conditions, indicating unburned hydrocarbons.

Figure 11 shows the measured temperature along the axis from the porous top to the chamber exit. In the low air flow rate of 6 L/min case, the flow temperature reaches its maximum earlier for the stainless steel porous burner than for the bronze burner. The result indicates that the hot spot of the stainless steel porous cap can efficiently preheat air/fuel so that the reactant gas can reach reasonably high temperature immediately after leaving the porous medium. Conversely, when the air flow rate goes up to 8 L/min, the high temperature in the bronze case moves upstream and occurs closer to the cap than occurs in the stainless steel case. At higher flow rate, the recirculation zone strengthens so that the air and fuel premixes more completely in the vicinity of the bronze porous media's top pulling the highest temperature zone upstream.

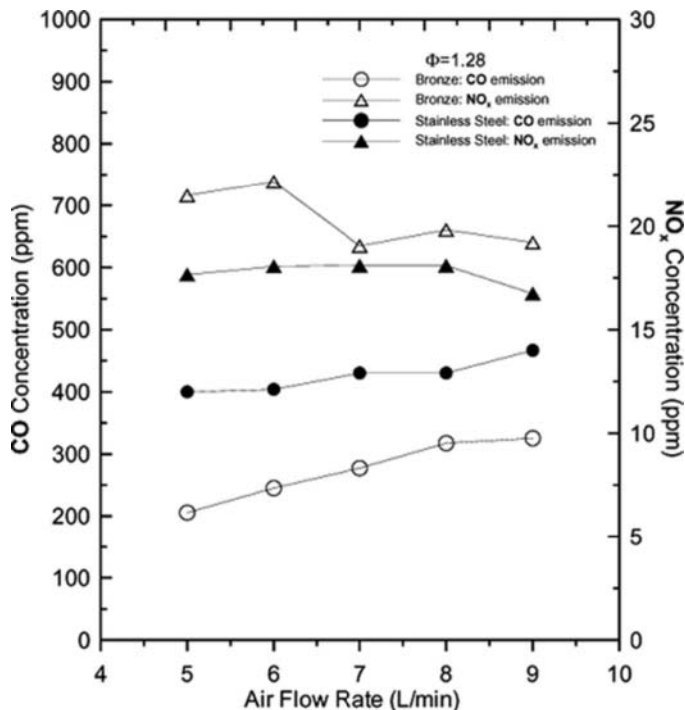


Figure 12 Typical CO and NO_x emissions from the stainless steel and bronze porous media combustors.

The combustors were operated for heat release rate varying from 295 to 665 W at fixed equivalence ratio. The CO and NO_x emissions over a range of air flow rate are presented in Figure 12 for different porous materials. CO emission at the center of the combustor exit plane for various air flow rates is between 100 and 450 ppm referring to 15% O₂, with higher values obtained at higher air flow rates. The shorter residence time at higher air flow rate is expected to increase the CO emission. The majority of CO emission is likely formed in the low temperature region. It is also likely that high air flow rates stretch the flame and cause local flame quench inside the chamber. The CO emission increases with air flow rate for both cases. The NO_x emissions distributes between 10–25 ppm, which is quite acceptable for liquid fuel combustors. In the stainless steel case, the NO_x emissions is much lower and the CO emission is higher than in the bronze case as would be expected from the differences noted in flame structure and temperature profiles.

Combustion in Combustors of Different Porous Sizes

As discussed before, the porous medium plays an important role in the spread of the liquid fuel as a thin film and in stabilizing the flame by transferring

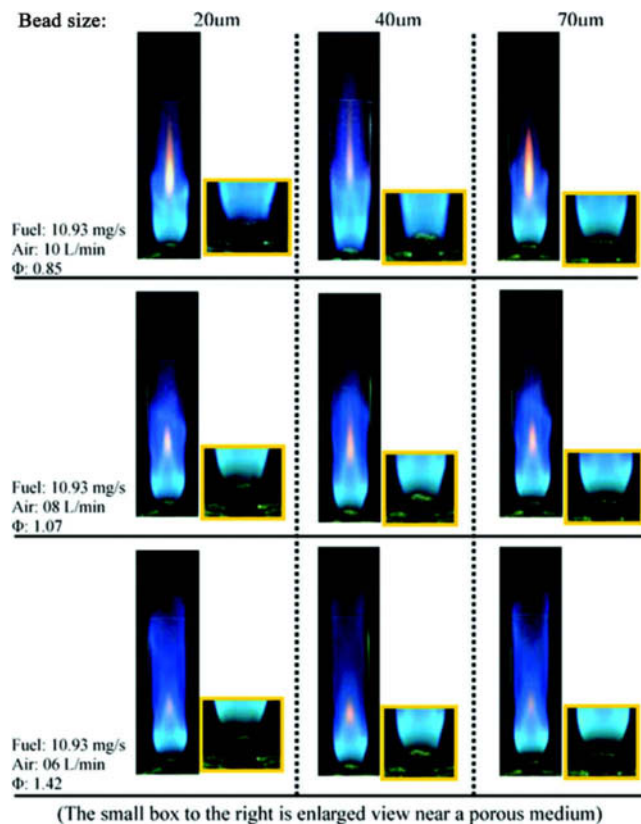


Figure 13 Images of flame shape and anchoring behavior for combustor with different bronze bead sizes.

heat from the flame zone to the fuel. It appears, therefore, that the porosity and thermal conductivity of the porous cap are important parameters. Generally, the large bead-size porous medium has relatively large porosity and lower thermal conductivity (K_{cond}) according to the Katz and Thompson's formula: $K_{cond} = A_c(r_u/r_s)^{2-d_f}$, where $A_c \sim 1$, and r_u and r_s are, respectively, the bead sizes characteristic of the upper and lower limits of the self-similar regime and $2 < d_f < 3$ is the fractal dimension.

Theoretically, the thermal conductivity of the porous medium could influence the fuel vaporization rate and the combustion phenomena in the chamber. Figure 13 shows the flame structures and flame anchoring positions for air flow rate from 6 to 10 L/min (corresponding to equivalence ratio from 0.85 to 1.42) for bronze porous media with three bead size (20, 40, and 70 μm). The results indicate that the flame structure and flame anchoring position do not change much with air flow rate nor with bead size. Basically, the reaction zone structures remain two-layer flames with corresponding flame anchors atop the porous cap. Furthermore, the operating window of the different bead size varies only moderately.

Figure 14 shows the stability range of heptane/air combustion in the bronze porous cap combustor with different pore sizes. The larger bead size produces a smaller stable operation range due to the relatively lower thermal conductivity and thermal mass so its ability to absorb heat from the flame for fuel vaporization is lower compared to the smaller bead size case. Moreover, the flame from the bigger

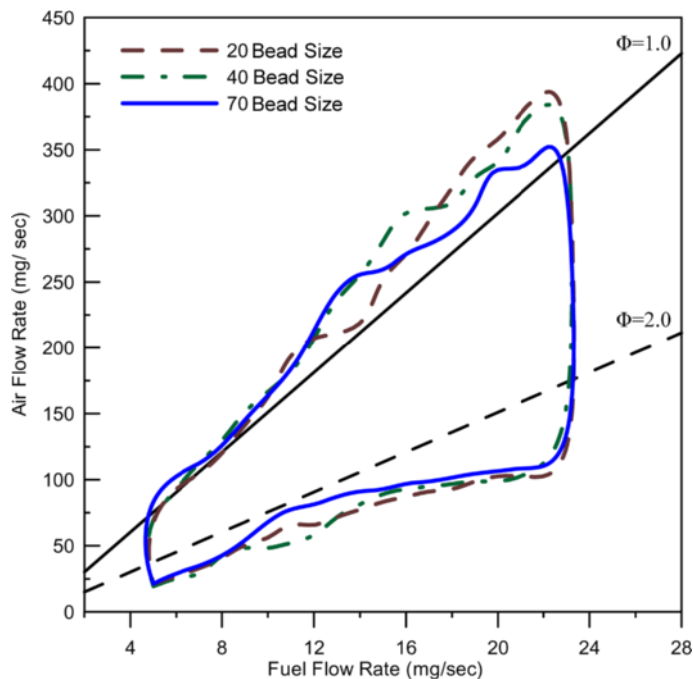


Figure 14 Stable operational envelopes for combustor with different bronze bead sizes.

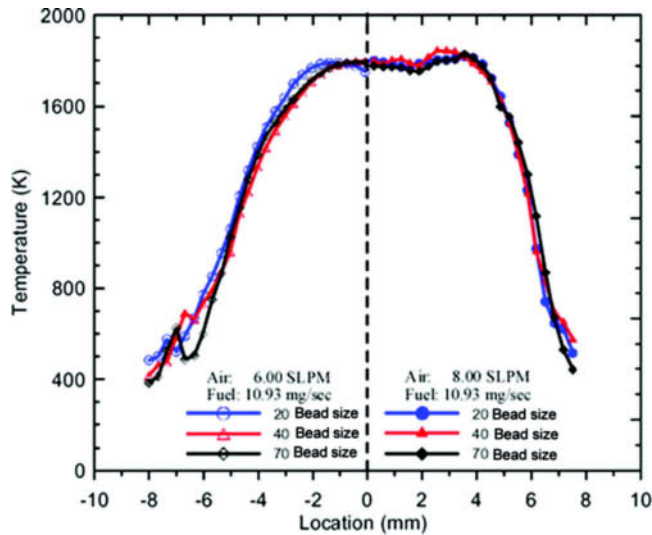


Figure 15 Temperature distributions at the combustor exit for different bead sizes. (Right-hand side: air 6 L/min; left-hand side: air 8 L/min).

bead size combustor is more sensitive to external perturbation in part because the fuel spread is dominated by external air flow rather than capillarity. In addition to having a wider stable operating range, the 20 μm bead size medium has the capability of running in the fuel-lean regime due to its relatively high thermal conductivity and uniform temperature distribution on surface.

Despite these differences, Figure 15 shows that the exit temperature distribution of combustors with the three bead sizes are similar, indicating that the heat release is independent of bead size. In addition, the bottom boundaries of the operation window for the three different bead sizes almost coincide. This lower limit defines the occurrence of the volcano flame where the liquid fuel pools in the chamber. This phenomenon, therefore, is also independent of bead size. Overall, the results indicates that bead size has an important but secondary effect on the combustion.

CONCLUSIONS

A new meso-scale liquid fuel film combustor with central porous inlet has been developed and tested. Specifically the effects of porous material and bead size on the flame structure and combustion characteristics are examined in this study. The results show that flame structure and the corresponding stabilization mechanism are different between a stainless steel and a bronze porous medium combustor due to their different thermal properties. In the stainless steel case, a hot spot exists on the top of porous medium and the flame anchor locates on the lateral surface of the porous cap. In the bronze case, the recirculation zone above the porous cap offers a low velocity field to help anchor the flame.

Chemiluminescence measurements illustrate the OH^* , CH^* , C_2^* concentration profiles at the base of flame anchor, and the deconvoluted line-of-sight images clearly reveal a tribrachial flame structure at the flame base. The location of the tribrachial flame dictates the characteristic stabilization mechanism of the porous combustor with different porous materials. As to the effects of bead sizes, there is no obvious difference in flame structure and flame anchoring position, but the stable operating ranges of a porous combustor decrease with an increase in the bead size due mainly to its effect on thermal conductivity.

REFERENCES

- Ahn, J., Eastwood, C., Sitzki, L., and Ronney, P. (2005) Gas-phase and catalytic combustion in heat-recirculating burners. *Proc. Combust. Instit.*, **30**, 2463–2472.
- Cheng, T.S., Wu, C.-Y., Li, Y.-H., and Chao, Y.-C. (2006) Chemiluminescence measurements of local equivalence ratio in a partially premixed flame. *Combust. Sci. Technol.*, **178**, 1821–1841.
- Dasch, C.J. (1992) One-dimensional tomography: a comparison of Abel, onion-peeling, and filtered backprojection methods. *Appl. Optics*, **31**, 1146–1152.
- Dunn-Rankin, D., Leal, E.M., and Walther, D.C. (2005) Personal power systems. *Prog. Energy Combust. Sci.*, **31**, 422–465.
- Durisch, W., Bitnar, B., Roth, F., and Palfinger, G. (2003) Small thermophotovoltaic prototype systems. *Sol. Energy*, **75**, 11–15.
- Fuse, T., Kobayashi, N., and Hasatani, M. (2005) Combustion characteristics of ethanol in a porous ceramic burner and ignition improved by enhancement of liquid-fuel intrusion in the pore with ultrasonic irradiation. *Exp. Therm. Fluid Sci.*, **29**, 467–476.
- Fernandez-Pello, A.C. (2003) Micropower generation using combustion: Issues and approaches. *Proc. Combust. Instit.*, **29**, 883–899.
- Kaiser, S., Kyritsis, D.C., Dobrowolski, P. Long, M.B., and Gomez, A. (2003) The electro-spray and combustion at the mesoscale. *J. Mass Spectrom. Soc. Jpn.*, **51**, 42.
- Kaplan, M., and Hall, M.J. (1995) The combustion of liquid fuels within a porous media radiant burner. *Exp. Therm. Fluid Sci.*, **11**, 13–20.
- Kim, N.I., Kato, S., Kataoka, T., Yokomori, T., Maruyama, S., Fujimori, T., and Maruta, K. (2005) Flame stabilization and emission of small Swiss-roll combustors as heaters. *Combust. Flame*, **141**, 229–240.
- Kyritsis, D.C., Roychoudhury, S., McEnally, C.S., Pfefferle, L.D., and Gomez, A. (2004) Mesoscale combustion: A first step towards liquid fueled batteries. *Exp. Therm. Fluid Sci.*, **28**, 763–770.
- Lawn, C.J. (2000) Distributions of instantaneous heat release by the cross-correlation of chemiluminescent emissions. *Combust. Flame*, **123**, 227–240.
- Liedtke, O., and Schulz, A. (2003) Development of a new lean burning combustor with fuel evaporation for a micro gas turbine. *Exp. Therm. Fluid Sci.*, **27**, 363–369.
- Marbach, T., and Agrawal, A.K. (2005) Experimental study of surface and interior composite porous inert media. *J. Eng. Gas Turb. Power*, **127**, 307–313.
- Marbach, T., Sadasivuni, V., and Agrawal, A.K. (2007) Investigation of a miniature combustor using porous media surface stabilized flame. *Combust. Sci. Technol.*, **179**, 1901–1922.
- Najm, H.N., Paul, P.H., Mueller, C.J., and Wyckoff, P.S. (1998) On the adequacy of certain experimental observables as measurements of flame burning rate. *Combust. Flame*, **113**, 312–332.

- Norton, D.G., and Vlachos, D.G. (2005) Hydrogen assisted self-ignition of propane/air mixtures in catalytic microburners. *Proc. Combust. Instit.*, **30**, 2473–2480.
- Pham, T.K., Dunn-Rankin, D., and Sirignano, W.A. (2007) Flame structure in small-scale liquid film combustor. *Proc. Combust. Instit.*, **31**, 3269–3275.
- Qin, X., Puri, I.K., and Aggarwal, S.K. (2002) Characteristics of lifted triple flames stabilized in the near field of a partially premixed axisymmetric jet. *Proc. Combust. Instit.*, **29**, 1565–1572.
- Qiu, K., and Hayden, A.C.S. (2007) Thermophotovoltaic power generation systems using natural gas-fired radiant burners. *Sol. Energy Mater. Sol. Cells*, **91**, 588–596.
- Shu, Z., Krass, B.J., Choi, C.W., Aggarwal, S.K., Katta, V.R., and Ouri, I.K. (1998) An experimental and numerical investigation of the structure of steady two-dimensional partially premixed methane-air flames. *Proc. Combust. Instit.*, **27**, 625–632.
- Sirignano, W.A., Pham, T.K., and Dunn-Rankin, D. (2002) Miniature-scale liquid-film-film combustor. *Proc. Combust. Instit.*, **29**, 925–931.
- Sirignano, W.A., Stanchi, S., and Imaoka, R. (2005) Linear analysis of a liquid-film combustor. *J. Propul. Power*, **21**, 1075–1091.
- Spadaccini, C.M., Mehra, A., Lee, J., Zhang, X., Lukachko, S., and Waitz, I.A. (2003) Preliminary development of a hydrocarbon-fueled catalytic micro-combustor. *Eng. Gas Turbines Power*, **125**, 709–719.
- Tseng, C.-J., and Howell, J.R. (1996) Combustion of liquid fuels in a porous radiant burner. *Combust. Sci. Technol.*, **112**, 141–161.
- Wang, Y., Yang, V., and Yetter, R. A., (2004) Combustion in meso-scale combustors II: numerical simulation. *AIAA Paper*, 2004-0981.
- Weinberg, F.J., Rowe, D.M., Min, G., and Ronney, P.D. (2002) On thermoelectric power conversion from heat recirculating combustion systems. *Proc. Combust. Instit.*, **29**, 941–947.
- Yuasa, S., Oshimi, K., Nose, H., and Tennichi, Y. (2005) Concept and combustion characteristics of ultra-micro combustors with premixed flame. *Proc. Combust. Instit.*, **30**, 2455–2462.